InSAR full-resolution analysis of the 2017–2018 M > 6 earthquakes in Mexico

Simone Atzori[a],[*], Andrea Antonioli[a], Cristiano Tolomei[a], Vincenzo De Novellis[b], Claudio De Luca[b], Fernando Monterroso[b]

[a] *Istituto Nazionale di Geofisica e Vulcanologia, Rome, Italy*
[b] *Istituto per il Rilevamento Elettromagnetico dell'Ambiente, Naples, Italy*

ABSTRACT

The present study analyzes the sequence of 4 important earthquakes occurred in Mexico from September 2017 to February 2018, exploiting the large availability of InSAR data and analytical models, with a twofold goal: to privede new solutions for seismogenic sources, completely independent from seismological data, and to discuss methodological aspects related to the non-linear and linear inverse problem. We review and update an earlier study, focused on the concept of resolution, showing the level of detail achievable in the investigation of the slip distribution based on geodetic observations, according to data availability, fault locations and event magnitudes. We further give new insights into the relationship between fault resolution and parameter uncertainty, demonstrating that a realistic assessment is strictly related to a proper fault subdivision. We eventually discourage the use of qualitative approaches, such as the checkerboard test, to evaluate the data resolving power and suggest the adoption of quantitative indicators, like the Dirichlet Spread Function, normalized, easy to calculate and mathematically robust.

1. Introduction

In 2017, 2018 Mexico was affected by several moderate-to-great magnitude earthquakes characterized by different intensities, mechanisms, depths and locations: the offshore M 8.2 Tehuantepec, also known as Chiapas or Pijijiapan, event, a deep earthquake with a normal mechanism occurred on September 8, 2017; the M 7.1 Puebla-Morelos, also with normal mechanism, occurred on September 19, 2017, about 120 km S-E of Mexico City; the M 6.1 Ixtepec, a shallow event with a predominantly normal mechanism, occurred on September 23, 2017 and the M 7.2 Oaxaca earthquake, occurred on February 16, 2018, with a thrust mechanism characteristic of subduction zones. We will refer to these events also as *eq1_m8.2*, *eq2_m7.1*, *eq3_m6.1* and *eq4_m7.2*, adopting the magnitudes released by USGS (Fig. 1 and Table 1).

In this paper we review all these events providing new source solutions based on an unprecedented and large amount of InSAR data. Some of these events have already been investigated by other authors, specifically *eq1_m8.2* and *eq2_m7.1*, who exploited local and global seismic waveform inversion, tsunami observations, DART (Deep-ocean Assessment and Reporting of Tsunamis) and GPS data (Chen et al., 2018; Heidarzadeh et al., 2018; Melgar et al., 2018a, 2018b; Gusman et al., 2018; Ramìrez-Herrera et al., 2018; Adriano et al., 2018). All

these analyses make no or marginal use of InSAR data.

InSAR data used in this work are obtained from the processing of Sentinel-1 (European Space Agency) and ALOS-2 (Japan Aerospace Exploration Agency) satellites; in the analysis of *eq1_m8.2*, the overall dataset has been corrected with GACOS (Generic Atmospheric Correction Online Service for InSAR; Yu et al., 2017; Yu et al., 2018) to mitigate the impact of atmospheric artifacts and a quantitative analysis of the GACOS impact is presented in Section 5.

The objective of this work is to provide new source models, based on InSAR data for all the events, through the application of the full-resolution algorithm already presented in Atzori and Antonioli (2011), with a strict comparison with models coming from a typical fault subdivision in patches of equal size.

While "resolution" is generally used to qualitatively indicate the spatial detail retrievable in the fault subdivision, in this study is adopted quantitatively, as the diagonal of the model resolution matrix (Menke, 1989), better explained in Section 3.

The idea of accounting for the resolution in geodetic data modeling has already been proposed by many authors, either through qualitative approaches, such as the checkerboard test, or through more powerful tools, as the model resolution matrix (Sagiya and Tatcher, 1999; Reilinger et al., 2000; Wright et al., 2003; Funning et al., 2005; Biggs et al., 2006; Cheloni

---
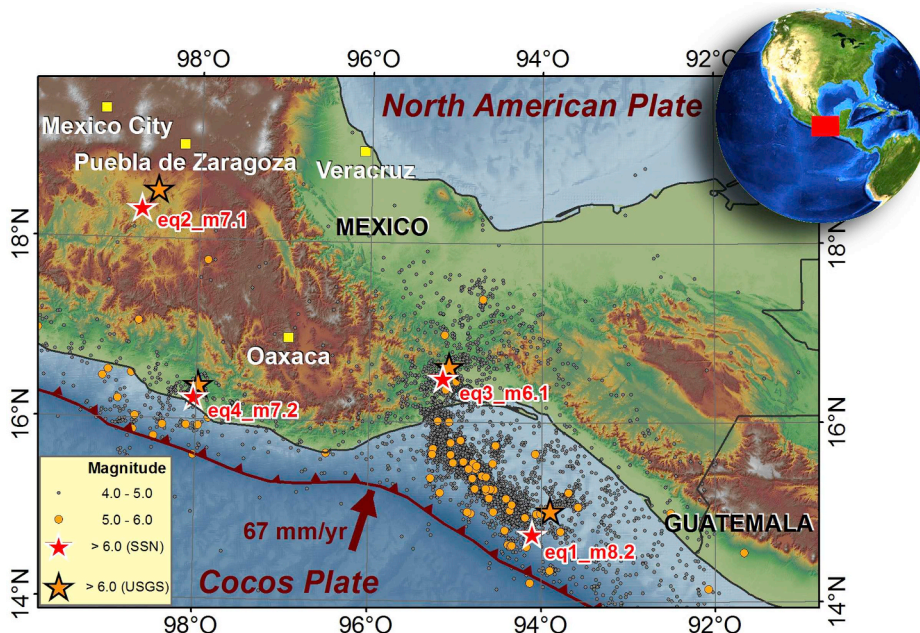
Fig. 1. One year of seismicity (September 2017–2018), for the investigated area, with highlighted the four M 6 + events analyzed in this work. Epicenters from Servicio Sismológico Nacional (Mexico) and mainshock locations also from USGS (orange stars).

Table 1

Event focal mechanisms and centroid depths from Global Centroid-Moment-Tensor (National Science Foundation), USGS and Servicio Sismològico Nacional (Mexico) catalogs, compared with the solutions of this study, obtained from linear inversion (Figs. 2–5). For *eq2_m7.1* both focal planes are reported, as they are both present in literature, with the preferred solution of this study.

Catalog	Magnitude	Strike	Dip	Rake	Depth
eq1_m8.2 (September 9, 2017)					
GCMT	8.2	318	78	−93	44.8
USGS	8.2	314	73	−100	45.5
SSN	8.3	310	81	−98	60.5
This study (full-res)	8.0	317	73	−95	54.8
This study (eq. pat.)	7.9	317	73	−98	42.3
eq2_m7.1 (September 19, 2017)					
GCMT	7.1	109/300	46/44	−97/-83	51.0
USGS	7.1	108/299	47/44	−98/-82	50.5
SSN	7.1	111/302	47/44	−97/-82	45.5
This study (full-res)	7.0	302	46	−90	51.4
This study (eq. pat.)	6.9	302	46	−90	50.3
eq3_m6.1 (September 23, 2017)					
GCMT	6.0	265	47	−65	12.8
USGS	6.1	234	38	−110	13.5
SSN	6.1	254	30	−80	11.5
This study (full-res)	6.0	258	50	−68	8.5
This study (eq. pat.)	6.0	258	50	−68	8.2
eq4_m7.2 (February 16, 2018)					
GCMT	7.2	292	13	83	20.0
USGS	7.2	297	12	91	25.5
SSN	7.2	291	10	91	11.5
This study (full-res)	7.0	292	13	80	17.4
This study (eq. pat.)	7.0	292	13	80	17.5

et al., 2010; Pritchard et al., 2002; Page et al., 2009; Custodio et al., 2009; Fialko et al., 2005 and many others). In Atzori and Antonioli (2011) a new algorithm was proposed to find an optimal fault subdivision, intended as a fault subdivision with the highest number of patches without falling into a system over-parametrization. In the Supplementary section "Full-resolution algorithm description" the algorithm steps are recovered from Atzori and Antonioli (2011), with a small improvement to include the effect of a variable rake. In addition, we propose a new quantitative assessment of the overall resolution, based on the Dirichlet Spread Function and shown, in a normalized form, for all the slip distributions.

2. InSAR and GPS data processing

Sentinel-1 and ALOS-2 images have been processed with the two-pass technique (Massonnet and Feigl, 1998). Sentinel-1 images were processed at IREA using the Parallel Small BAseline Subset (P-SBAS) (Casu et al., 2014) processing chain for Sentinel-1 dataset. The seismic sequence, composed of the four biggest earthquakes, was imaged with a 6-day revisit time and with the Interferometric Wide Swath (IWS) acquisition mode, referred to as Terrain Observation with Progressive Scans (TOPS) (De Zan and Monti Guarnieri, 2006). Particularly, to cover the whole area affected by seismic events we exploited five descending (70, 172, 99, 26, 143) and two ascending orbits (5, 107). The generated interferograms underwent a multilook operation (5 and 20 pixels along the azimuth direction and range, respectively) to finally lead to a ground pixel size of about 70 by 70 m. The phase unwrapping procedure used for S1 interferograms was the Minimum Cost Flow (Costantini, 1998; Costantini and Rosen, 1999). ALOS-2 images were processed at INGV with SARscape® (sarmap, CH); they were acquired in ScanSAR mode to cover the *eq1_m8.2* event, including *eq3_m6.1*, and strip map mode to cover *eq2_m7.1*. Interferograms were filtered with the Goldstein filter (Goldstein et al., 1998), unwrapped with a Minimum Cost Flow algorithm, then geocoded with a spatial resolution of 180 m. The complete list of interferograms is shown in Table 2. Both InSAR processors used the SRTM DEM, version 4 (Jarvis et al., 2008), to isolate the topographic phase contribution.

Only for *eq1_m8.2*, characterized by a low s.n.r. and strong atmospheric contributions, we corrected all Sentinel-1 and ALOS-2 interferograms with the GACOS approach (Yu et al. 2017, 2018). The impact of this corrections, important for some pairs and negligible for others, is shown in the Supplementary Fig. S1. To further increase the s.n.r. We averaged two groups of three independent ALOS-2 pairs, belonging to descending tracks 150 and 151; this reduced the number of InSAR datasets to investigate the *eq1_m8.2* source to 11. The complete list of maps used to constrain the earthquake sources is reported in Table 2: with the only exception of *eq2_m7.1*, all InSAR pairs are independent, i.e. no master or slave acquisitions are repeated in any image combination.

GPS data were obtained from the Nevada Geodetic Laboratory website (Nevada Geodetic Laboratory, 2019) an *ad hoc* code was developed in I.D.L. (Interactive Data Language, from Harris Geospatial

Table 2
List of all InSAR maps used to model the four events; some images belonging to the track have been averaged into a single one.

Satellite	Master-Slave	Orbit	Track	B. perp
	eq1_m8.2 (September 9, 2017)			
ALOS-2	25/07/2017–28/11/2017	Desc	152	31
ALOS-2	20/07/2017–28/09/2017	Desc	151	72
	22/06/2017–23/11/2017			76
	31/08/2017–12/10/2017			6
	Alos 151 mean			–
ALOS-2	08/04/2017–09/09/2017	Desc	150	414
	03/12/2016–02/12/2017			65
	20/05/2017–21/10/2017			247
	Alos 150 mean			–
ALOS-2	24/07/2017–27/11/2017	Desc	149	69
ALOS-2	14/08/2017–10/09/2017	Asc	55	85
Sentinel-1	14/07/2017–12/09/2017	Desc	70	92
Sentinel-1	07/09/2017–13/09/2017	Desc	172	55
Sentinel-1	02/09/2017–20/09/2017	Desc	99	25
Sentinel-1	28/08/2017–15/09/2017	Desc	26	77
Sentinel-1	08/09/2017–20/09/2017	Asc	5	45
Sentinel-1	03/09/2017–15/09/2017	Asc	107	60
	eq2_m7.1 (September 19, 2017)			
Sentinel-1	17/09/2017–23/09/2017	Desc	143	9
Sentinel-1	05/09/2017–23/09/2017	Desc	143	66
ALOS-2	22/02/2017–04/10/2017	Asc	57	122
ALOS-2	06/09/2017–20/09/2017	Asc	57	210
	eq3_m6.1 (September 23, 2017)			
ALOS-2	20/07/2017–28/09/2017	Desc	151	72
	22/06/2017–23/11/2017			76
	31/08/2017–12/10/2017			6
	Alos 151 mean			–
ALOS-2	03/12/2016–02/12/2017	Desc	150	65
	20/05/2017–21/10/2017			247
	Alos 150 mean			–
Sentinel-1	19/09/2017–25/09/2017	Desc	172	23
Sentinel-1	21/09/2017–03/10/2017	Asc	107	28
	eq4_m7.2 (February 16, 2018)			
Sentinel-1	05/02/2017–17/02/2017	Asc	5	378
Sentinel-1	14/02/2017–20/02/2017	Desc	143	5

Solutions) to get the data, calculate the static offset averaging 5 to 10 days before and 2 to 5 days after the event, calculate the data variance and format the results for the modeling ingestion. For the Ixtepec event (*eq3_m6.1*) GPS data are not considered because they are not available in the source proximity.

3. Data modeling and full-resolution algorithm

Before modeling, raster InSAR maps are sampled to create the point shapefiles used in the inversion, with extents and resolutions shown in Supplementary Fig. S2. The sampling distance, especially in the fault near field, is set to be reasonably redundant compared to the smallest fault element detected with the full-resolution approach, as verified *a posteriori* by comparing Fig. S2 with Figs. 2–5.

Modeling of InSAR and GPS data is carried out with a consolidated two-step approach: a preliminary non-linear optimization, based on the Levemberg-Marquardt algorithm (Marquardt, 1963), to define fault geometry and rupture mechanisms, followed by a linear inversion to get the slip distribution. Both steps are carried out in a least square sense. The non-linear global minimization is implemented with multiple restarts to avoid the cost function getting trapped into local minima; parameter uncertainty and trade-offs are also calculated, running 100 inversions of datasets perturbed by *ad hoc* noise, correlated in space. The linear inversion is performed with bounded or fixed rake, depending on the event magnitude, and a non-negative inequality constraint.

Together with source parameters, both inversions infer the contribution of possible orbital ramps or quadratic surfaces for InSAR data. The overall modeling is conducted with a modified version of the SARscape ® modeling module.

For non-linear inversion, we minimize the following cost function, which is the total of the cost functions $CF(D)$ of every dataset:

$$Cost\ function\ =\ \sum CF(D) = \sum_D \left(\frac{w_D}{N_D} \cdot \sum (\mathbf{e}_D^T \mathbf{W}_{e,D} \mathbf{e}_D) \right)$$

where, for every dataset D, the vector $\mathbf{e}$ contains the point-by-point difference ($d_{i,obs} - d_{i,mod}$) between the observed and the predicted values, N is the number of observations, $\mathbf{W}_e$ is the data weighting matrix and w_D is the dataset weighting coefficient. The matrix $\mathbf{W}_e$ is the inverse of the full variance-covariance matrix Cov($\mathbf{d}$) of the observed data $\mathbf{d}$

$$\text{Cov}(\mathbf{d}) = \begin{vmatrix} \sigma_1^2 & \sigma_{12} & ... \\ \sigma_{21} & \sigma_2^2 & ... \\ ... & ... & ... \end{vmatrix}$$

containing the data variance in the diagonal and, in the off-diagonal, a covariance exponentially decreasing with the distance

$$\sigma_{ij} = cov(0) \cdot e^{-\frac{d_{ij}}{k}}$$

where $cov(0)$ is the covariance at zero distance, d_{ij} the distance between the i-th and j-th points and k is the decaying factor, setting the distance above which data are substantially uncorrelated. Values for σ_i^2, $cov(0)$ and k are assumed on a statistical basis: $4\ cm^2$, $3.5\ cm^2$ and $4.5\ km$, respectively. The weighting coefficient w_D is initially assumed to be equal to 1. In a purely theoretical case, it should occur that

$$CF(D)_{theor} = \frac{1}{N} \cdot \sum (\mathbf{e}^T \mathbf{W}_e \mathbf{e}) = 1$$

but in practice, $CF(D)$ is always $\neq 1$, due to the impossibility of a formal assessment of Cov($\mathbf{d}$). After the first inversion, w_D is calculated to have $CF(D) \cdot w_D = CF(D)_{theor} = 1$. A second inversion is then run introducing w_D as stretching factor of Cov($\mathbf{d}$), according to

$$\text{Cov}(\mathbf{d})_{new} = \frac{1}{w_D} \text{Cov}(\mathbf{d})$$

A new solution will be reached, with different residuals and allowing a new assessment of w_D, used as uncertainty stretching factor in the next iteration; in few iterations, w_D values get stable and the cost function contribution of every dataset perfectly balanced.

Dataset weights are then maintained for the linear inversion, which we run to retrieve the fault slip distribution, $\mathbf{m}^{est}$, by solving the weighted and damped least-square linear system

$$\mathbf{m}^{est} = [\mathbf{G}^T \mathbf{W}_e \mathbf{G} + \varepsilon^2 \mathbf{W}_m]^{-1} \mathbf{G}^T \mathbf{W}_e \mathbf{d} = \mathbf{G}^{-g} \mathbf{d}$$

where ε is the empirical coefficient controlling the importance of $\mathbf{W}_m$, the parameter weighting matrix based on the Laplacian operator, $\mathbf{G}$ is the design matrix and $\mathbf{W}_e$ is again the inverse of Cov($\mathbf{d}$), covariance matrix of the data $\mathbf{d}$, multiplied by $1/w_D$, as for the non-linear inversion; $\mathbf{G}^{-g}$ is the generalized inverse of the linear system (Menke, 1989).

The full-resolution results are based on the model resolution matrix $\mathbf{R}$, defined as $\mathbf{G}^{-g} \mathbf{G}$ and the algorithm details, first presented in Atzori and Antonioli (2011), are also reported in the supplementary section "Full-resolution algorithm description", extended to the case of variable rake.

In addition, we introduce a new indicator for the difference between the two solutions (fixed vs variable patch dimensions): the normalized Dirichlet Spread Function of $\mathbf{R}$

$$norm.\ spread(\mathbf{R}) = \frac{\|\mathbf{R} - \mathbf{I}\|_2^2}{N}$$

that is the L_2 norm of the difference between the model resolution matrix $\mathbf{R}$ and the identity matrix I (Menke, 1989), normalized with the number of free parameters N. This function ranges from 0, for a perfectly resolved system, to 1 for a completely unresolved system (a purely theoretical case). In the next sections, slip distributions with a regular subdivision and the full-resolution algorithm are provided,
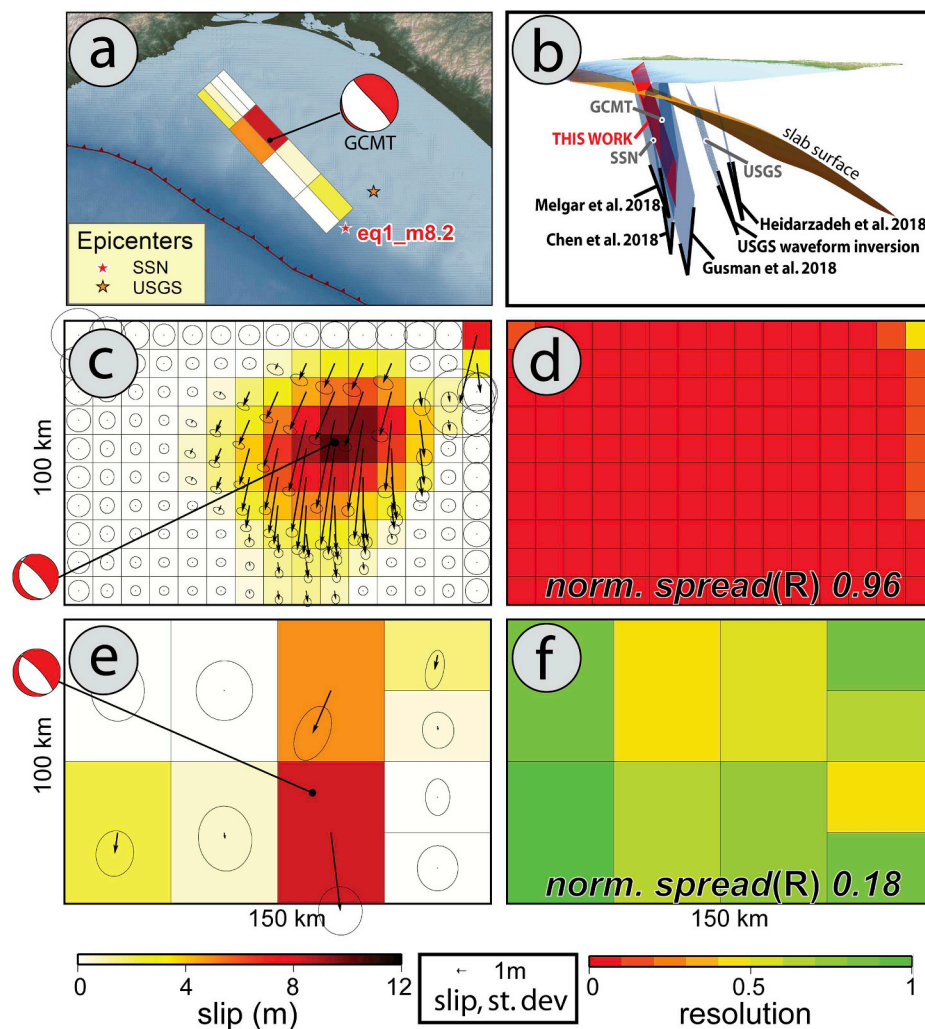
Fig. 2. (a) Planimetric fault view with SSN and USGS epicenters and the global CMT centroid location; (b) 3D fault and slab surface view, compared with published solutions and hypocenters from SSN, USGS and GCMT; (c) and (e) slip distributions with the 1-sigma uncertainty and InSAR centroid locations; (d) and (f), distribution of resolution values, for the two subdivisions, with the normalized Dirichlet Spread Function values, ranging from 0 (perfectly resolved) to 1 (completely unresolved).

showing that the same fit can be obtained with smaller values of the *norm. spread*(**R**) function, i.e. with a consistently better resolved set of parameters.

The difference concerns not only the reduced number of parameters, but also the reliability of the solution: slip distributions are less affected by mathematical artifacts and the uncertainty analysis is more robust. In the following section, slip and uncertainty distributions for full-resolution and equally sized patches, either with fixed or variable rake, are presented for the four events, completed with the resolution values and the *norm. spread*(**R**) of every solution.

4. Modeling results

4.1. The September 8, 2017, M 8.2 event

Despite its high magnitude, the offshore position and the source depth make it difficult to constrain the geometry of this fault: InSAR data only map the coseismic far field, where displacements do not exceed 0.2 m. In addition, strong atmospheric disturbances affect InSAR interferograms, masking the coseismic signal in some areas. At first glance, displacement maps show a weak signal, at places correlated with topography, unexpected deformation patterns and contradicting trends. For these reasons, all the available displacement maps have been corrected with GACOS data, described above (Supplementary Fig. S1). To

compensate for these discouraging conditions we have processed a large amount of InSAR pairs (Table 2): although the different line-of-sights prevent averaging them into a single displacement map with a reduced noise, the joint inversion of all datasets still provides a better constrained solution, completely independent from seismological data.

Several sources have already been proposed, based on: geodetic and teleseismic data (Chen et al., 2018, using only 2 InSAR Sentinel-1 tracks), teleseismic and tsunami observations (Heidarzadeh et al., 2018), GPS, strong motion and tsunami data (Melgar et al., 2018a), tide gauges and DART data (Gusman et al., 2018; Ramìrez-Herrera et al., 2018). All these solutions are initialized, or constrained, on the basis of available hypocenters or focal mechanisms, either from Servicio Sismológico Nacional of Mexico (SSN, 2018), USGS (USGS, 2017) or the global CMT catalog (Dziewonski et al., 1981; Ekström et al., 2012, Table 1). The scattered hypocenter locations naturally affect the spatial distribution of the proposed sources (Fig. 2b).

We carried out the first non-linear inversion with all parameters free, however the uncertainty analysis revealed the existence of two similar cost function minima corresponding to dip angles of 83°, less realistic but preferred in non-linear inversion, and 72° (Supplementary Fig. S3); we therefore constrained the source to have a dip angle of 73° as proposed by USGS (Table 3). Our best-fit source confirmed the existence of a shift between global and regional hypocenter solutions (Hjörleifsdóttir et al., 2016) (Fig. 2b).

Table 3
Best fit parameters, with relative standard deviation, coming from non-linear inversions.

Fault	Length (km)	Width (km)	Depth (km)	Dip (deg)	Strike (deg)	Rake (deg)	Slip (m)	Moment (N·m)	Mag
eq1_m8.2	117 (12)	112 (8)	13 (4)	73 [a]	317 (1)	−98 (1)	2.5 (0.4)	$1.00\ 10^{21}$	8.0
eq2_m7.1	48.3 (7.2)	10[b]	44 (2.0)	46 (2)	301 (5)	−90 (3)	1.7 (0.3)	$2.5\ 10^{19}$	6.9
eq3_m6.1	9.0 (0.9)	6 (1)	6 (1)	50 (3)	258 (5)	−68 (9)	0.8 (0.1)	$1.17\ 10^{18}$	6.0
eq4_m7.2	42.3 (1.2)	34 (1)	13 (1)	14 (1)	292 [a]	81 (2)	1.0 (0.1)	$4.2\ 10^{19}$	7.1

[a] Constrained with USGS focal mechanism.
[b] Constrained *a priori*.

After the non-linear inversion and the assessment of the parameter uncertainty and trade-offs (Supplementary Fig. S4), the slip distribution is calculated with fixed patches of 10 km, and with the full-resolution algorithm. Due to the event's high magnitude, we relaxed the rake variability allowing it to vary in a range of 30° around the best fit of −98°, in both cases. The two solutions, predicting equally well the observed data (see Supplementary Fig. S5), are shown in Fig. 2, with their resolution values and the *spread*(**R**).

With the exception of few patches, all the resolution values for the regular subdivision have values below 0.1. On the other hand, the full-resolution analysis reveals that the poor InSAR coverage makes it impossible to retrieve fault details smaller than ~30 km, in the best case: 10 patches are enough to predict the observed displacement and to infer the presence of an important slip between 42 and 60 km, with a mean value of ~8 m. This coarser distribution makes the centroid locations deeper than the regular subdivision, 54.8 vs 42.3 km, explained by the fact that the slip field is not fading at zero at bottom; this slip pattern is, in turn, only the consequence of the damping effect over nearly completely unresolved patches. The full-resolution centroid depth is the closest one to that provided by the Servicio Sismològico Nacional (Table 1). In spite of this coarseness, the distribution extending west of the SSN and USGS hypocenters suggests and confirms the lateral, westward, rupture propagation (Fig. 2).

4.2. The September 19, 2017, M 7.1 event

This second event also shows a weak signal, less than 10 cm, due to the source depth. In this case, only 4 InSAR and 1 GPS datasets are available, but we still can constrain the source geometry and provide indications about the slip distribution.

Several models have been proposed: the USGS broadband waveform inversion sets the best fit source in a SW-dipping plane (USGS, 2018); Melgar et al. (2018b) exploit regional broadband data, strong motion data and GPS, to define the NE-dipping plane as the preferred solution, though not fully resolved due to the lack of aftershocks clearly identifying the fault plane. To solve the ambiguity, we tried both nodal planes, leaving free all the parameters except for the width, showing a perfect trade-off with the slip; we found the NE-dipping normal fault slightly preferred in terms of data fit (see Supplementary Fig. S6 for the uncertainty analysis). In addition, the slip on the NE-dipping nodal plane is deeper than the SW one, making this solution more consistent with the hypothesis put forward by Melgar et al. (2018b) that the earthquake occurred in the upper part of the Cocos plate, in the vicinity of a rapid dip change of the slab, which goes from 5° to 75° in about 50 km, after underplating horizontally the North American plate for 200 km (Fig. 3b). This transition would generate stress conditions favorable to normal earthquakes dipping NE, as already occurred in other occasions, e.g. the 1999, M_w 7.0, Tehuacan earthquake (Singh et al., 1999).

In this case as well, the uniform subdivision and the full-resolution outcomes show the same data fit (Supplementary Fig. S7), but they give slightly different insights about the source. According to the local tectonic setting, a rupture occurring in the shallow part of the Cocos plate should show slip occurring downward from 50 km depth. The first distribution has most of the slip (darker patches in Fig. 3c, with values between 1.0 and 1.5 m) confined between 35 and 45 km, i.e. shallower than expected. Instead, the full-resolution analysis defines a mean slip of 0.5 m in large patches from 43 to 68 km depth, allowing to consider a rupture in the

upper part of the Cocos plate still possible; this difference in the slip distributions does not affect the centroid locations, suggesting that the slip decreasing to zero at the fault bottom in Fig. 3-c is still a mathematical artifact controlled by the Laplacian operator, as for the M 8.2 event.

The comparison between local (InSAR) and global (CMT) centroid locations confirms the existence of a N–S shift (13 km, at this latitude), already investigated by several authors (Weston et al. 2011, 2012; Hjörleifsdóttir et al., 2016).

4.3. The September 23, 2017, M 6.1 event

This event is covered by 7 InSAR datasets, 5 from ALOS-2 and 2 from Sentinel-1 satellites. As for *eq1_m8.2*, the 5 ALOS-2 datasets belonging to tracks 150 and 151 are averaged to get 2 displacement maps (Table 2). GPS data are not available for this area. ALOS-2 interferograms are the same as those of the *eq1_m8.2* case and they contain the superimposition of both earthquakes; in the inversion we take into account the contribution of the already modeled sources to isolate the signal related to the *eq3_m6.1* event.

In this case, the earthquake occurred at shallow depth in the crust of the North American plate, therefore we could exploit several interferograms to constrain all source parameters. We tested the whole strike range, to define the preferred fault plane between the two nodal planes. The best-fit is obtained with the NW-dipping plane with a normal mechanism and a minor left-lateral component (Table 3 and Supplementary Fig. S8 for the uncertainty analysis).

In this particular case, the source shallowness and its geometry make the full-resolution algorithm able to subdivide the fault into elements of size comparable with that of the equal subdivision, but only in the upper fault (Fig. 4c). The two solutions have a very similar data fit (see Supplementary Fig. S9); however, the variable-patch fault only required 36 fully resolved parameters, instead of 300 for the equal-patch fault. Centroids for both InSAR solutions are very close and the abovementioned shift between global and local solutions reaches a value of 25 km.

4.4. The February 16, 2018, M 7.2 event

This last event represents a typical thrust earthquake and it occurs at the interface between the Cocos and the North America plates. The event occurred in an area not already ruptured from previous megathrust events (Fig. 5a). The earthquake is modeled using two Sentinel-1 InSAR pairs, acquired from ascending and descending orbits, and a GPS dataset.

In this case as well, the amount of geodetic data allows for the inversion of all non-linear parameters, however the geometry of the source has an intrinsic trade-off between strike and rake angles: since the source is sub-horizontal, the same rupture direction can be achieved by rotating strike and rake in opposite directions (Fig. 5a). Fixing one of the two parameters was therefore necessary and we adopted strike 292°, according to the GCMT solution, leaving other parameters free (see Supplementary Fig. S10 for the uncertainty analysis).

The depth retrieved through the non-linear inversion, accounting also for its uncertainty, sets the source in agreement with the slab surface geometry proposed by Ferrari et al. (2012) (Fig. 5b)

The inversion for the slip distribution is conducted allowing the rake to vary in a range of 30°, centered on the best-fit value of 81° retrieved by
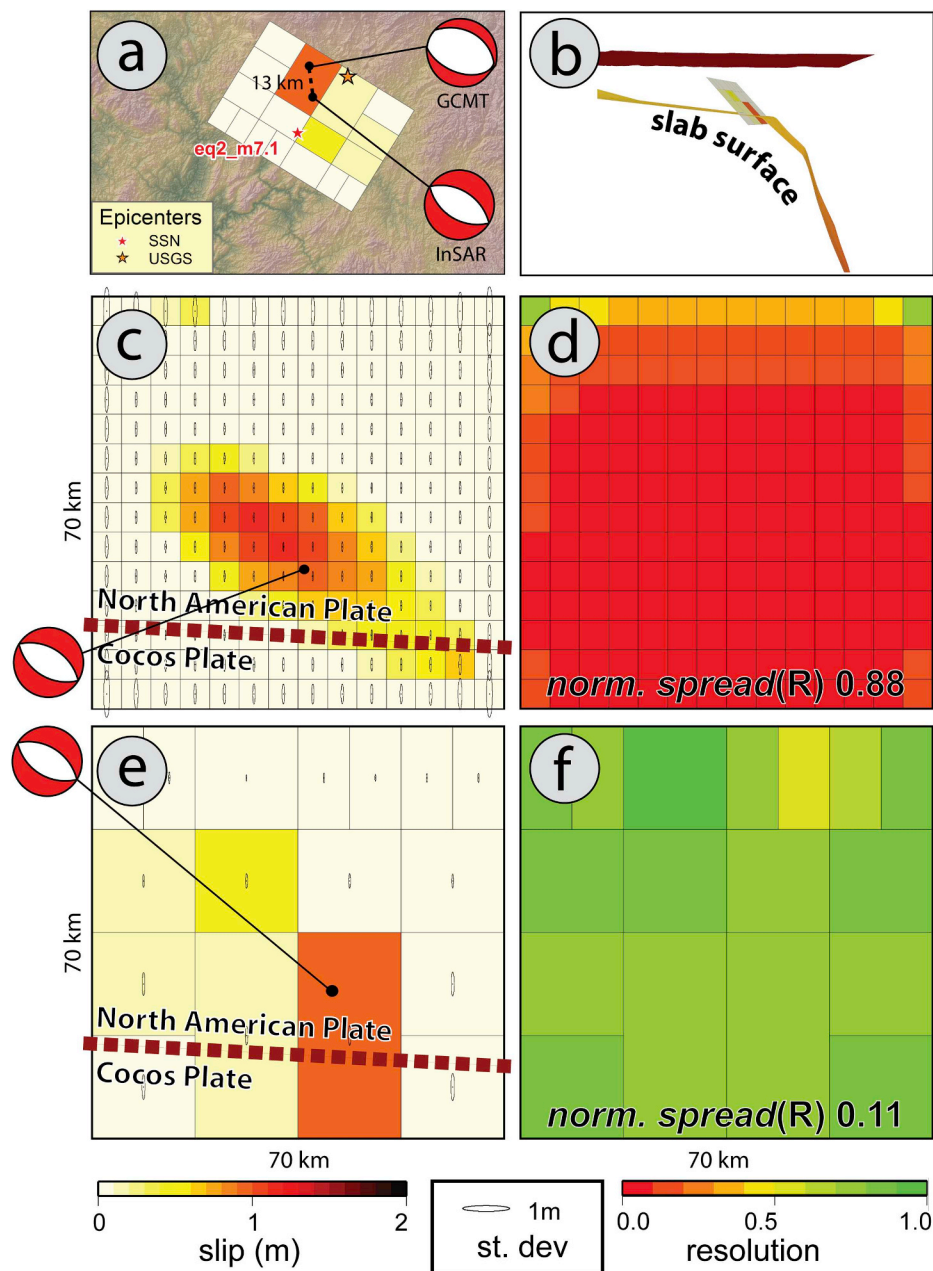
Fig. 3. (a) Planimetric fault view with SSN and USGS epicenters, global CMT and InSAR centroid locations and distance; (b) 3D slip distribution crossing the slab surface; (c), (d), (e) and (f) as in Fig. 2, with linear inversions carried out with a fixed rake and the intersection with the slab surface superimposed on the slip distributions.

the non-linear inversion. In this case as well, the two slip distributions are substantially equivalent, though the fully-resolved one shows a mean slip of about 0.5 m, reaching the fault bottom without giving the impression of an isolated slip pattern, as seen in the regular subdivision (Fig. 5c). The same data fit (shown in Supplementary Fig. 11) is reached with one order of magnitude difference in the number of parameters: 17 in the full-resolution inversion vs. 120 in the regular subdivision, showing again the numerical artifacts introduced with an over-determined redundant problem. The inversion strategy does not have an impact on the centroid locations, confirming also the northward shift of 24 km of the CMT global solution.

5. Discussion

In this work we considered a set of events with a wide range of magnitudes (from M 6.1 to M 8.2), focal mechanisms (normal and

thrust) and positions (shallow, deep, onshore, offshore), to get a comprehensive overview of the full-resolution algorithm impact in the modeling of geodetic data (InSAR and GPS).

Only for *eq1_m8.2*, the great offshore normal earthquake, we corrected the displacement maps with GACOS data, because of the strong impact of the atmosphere, sometimes well correlated with the topography. The GACOS impact is not univocal, nor is it easy to understand whether the corrected signal still contains residual atmospheric contributions; just in few cases, like the ALOS-2 pair 24/07/2017–27/11/2017, the removal of a signal highly correlated with topography is evident (Fig. S1). To quantitatively define the general impact of GACOS corrections, we compared the residuals between the predicted and the modeled data using the same input conditions: dataset number and weights, damping factor, full-resolution approach. While the two slip distributions (not shown) are nearly equal, some datasets show a slightly improved fit. We summarized this result in Fig. 6, obtained with the contributions of all the datasets: the
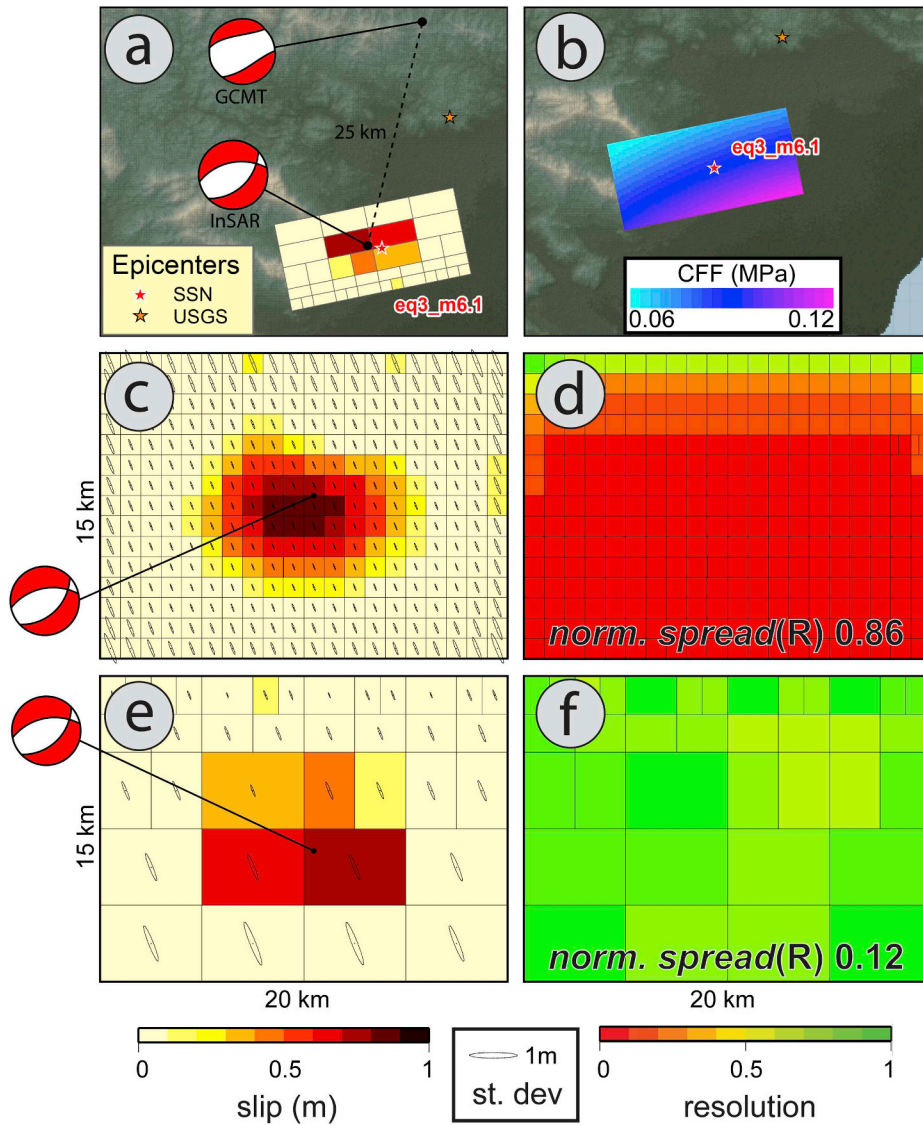
Fig. 4. (a) Planimetric fault view with SSN and USGS epicenters, global CMT and InSAR centroid locations and distance; (b) stress drop induced by the *eq1_m8.2* event; (c), (d), (e) and (f) as in Fig. 2, with linear inversions carried out with a fixed rake.

comparison between the two curves show that residuals are minimized above 8 cm and substantially reduced below 8 cm.

The increased fit can be attributed to the (partial) removal of non-tectonic signal features, that remain unmodeled without GACOS corrections.

A second important aspect of the full-resolution approach concerns the assessment of the source parameter uncertainties. If for non-linear inversion the presentation of probability distributions and trade-off scatter plots (Supplementary Figs. S4, S6, S8 and S10) completely describes the solution robustness, this completeness cannot be easily described after linear inversions for all the inverted parameters. In this case, their full variance-covariance matrix can be obtained through

$$\text{Cov}(\mathbf{m}) = \mathbf{G}^{-g}\text{Cov}(\mathbf{d})\mathbf{G}^{-g^T}$$

where Cov(**d**) is the full variance-covariance matrix of the geodetic data. The high number of parameters **m**, corresponding to the number of patches, makes it difficult to present the full Cov(**m**) matrix; sometimes the diagonal values, i.e. the parameter variances, are shown, but the rest of the matrix is ignored, although strong correlations may be present. The full-resolution subdivision, instead, minimizes the off-diagonal correlations and the variances truly describe the real precision of the slip values. This property of the full-resolution approach is

described in Fig. 7, where the covariance matrices Cov(**m**), for the two subdivisions, are shown after a normalization according to

$$\text{corr(i,j)} = \left| \frac{\sigma_{i,j}}{\sqrt{\sigma_{i,i}^2} \cdot \sqrt{\sigma_{j,j}^2}} \right|$$

brighter corr(i,j) values describe higher correlations between the *i*-th and *j*-th parameters.

Forcing the fault subdivision beyond the mathematical resolution generates clear off-diagonal correlations, while with the full-resolution subdivision this effect is minimized. It follows that the standard deviations shown in Figs. 2–5 as error ellipses, are more realistic for the full-resolution outcomes than the equally sized patches. A marginal consideration concerns the introduction of the variable rake in the new implementation of the full-resolution subdivision: as expected, the optimal subdivision with a variable rake implies a lower number of patches, since every patch contributes with two parameters (strike and dip-slip components). In Supplementary Fig. S12, the comparison between the two solutions is shown for *eq1_m8.2*.

We also suggest to using the full-resolution algorithm as an alternative to the checkerboard test, widely used to demonstrate whether a predefined fault subdivision can be truly resolved (see, for instance, the
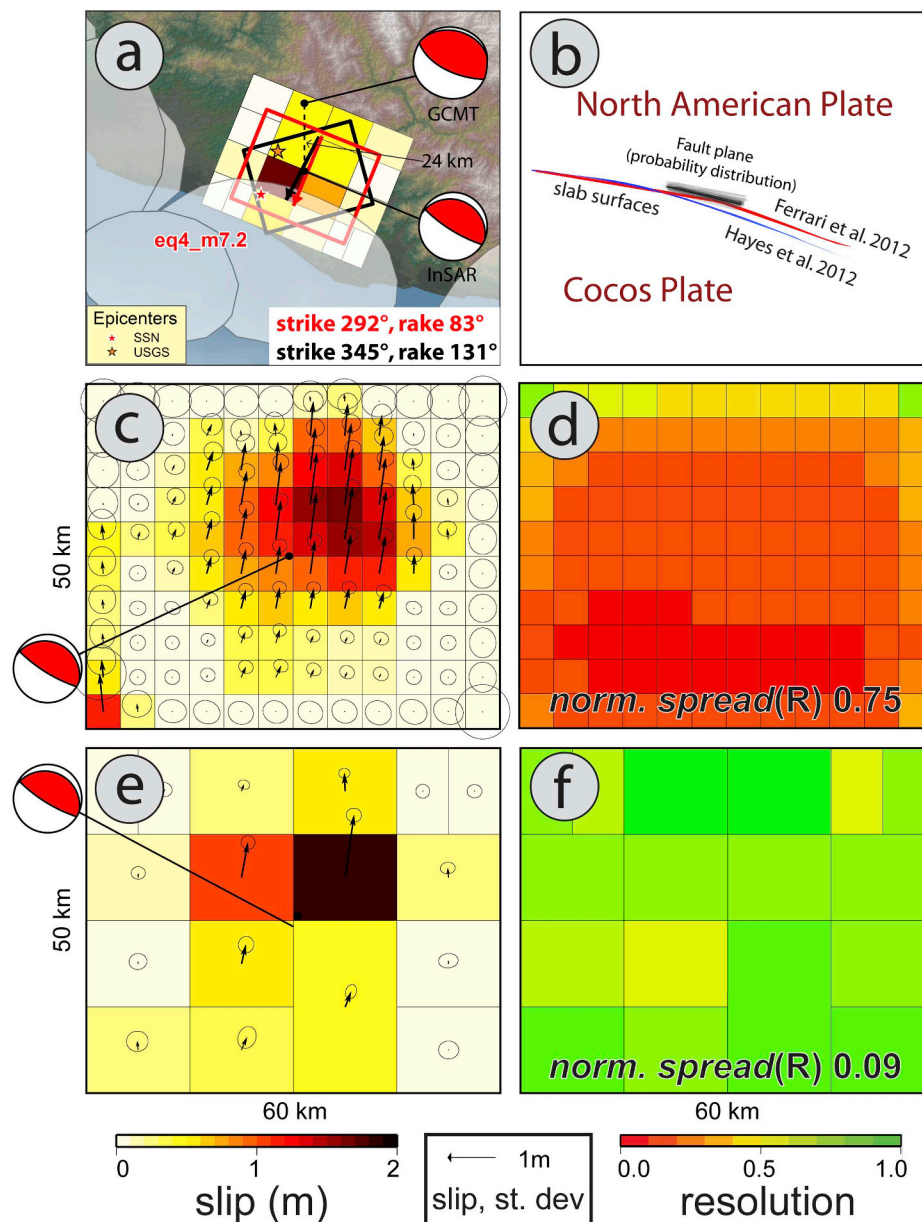
Fig. 5. (a) Planimetric fault view with SSN and USGS epicenters, global CMT and InSAR centroid locations and distance, strike vs. rake trade-off resulting from non-linear inversion and past megathrust events (transparent white); (b) best-fit source (black) and its probability distribution (gray) compared to slab surfaces (Ferrari et al.2012, Hayes et al. 2012); (c), (d), (e) and (f) as in Fig. 2, with the inversion carried out with variable rake.

supplementary material of Melgar et al., 2018a). The checkerboard test has an intrinsic limitation: it is carried out subdividing the fault into cells of equal size that are supposed to be *a priori* resolved, neglecting the strong resolution dependency on several factors, depth and geometric data coverage primarily: a checkerboard cell dimension, in the best case, is perfectly resolved only in a small area of the fault. We therefore encourage the use of simple and effective indicators, like the *spread*(**R**), to quantitatively reveal how much a fault, subdivided on the base of a checkerboard test, is totally under-resolved.

The analysis of this sequence, carried out with the full-resolution approach, confirmed certain hypothesis and provided new insights about the events. In particular, our slip distribution for the great normal Tehuantepec earthquake (*eq1_m8.2*), despite its unavoidable coarseness, supports the hypothesis that the earthquake ruptured the entire lithosphere well below the brittle to ductile transition depth in the Cocos slab, as suggested by Melgar et al. (2018b). Moreover, we proposed a fault location completely independent from seismological data, confirming the known spatial shift of the global-based solutions

compared to the regional ones (Weston et al., 2011, 2012; Hjörleifsdóttir et al., 2016): with the exception of the great normal event, GCMT solutions show a northward shift of about 24 km for *eq3_m6.1* and *eq4_m7.2*, having the same latitude, and of 13 km for *eq2_m7.1*. For *eq2_m7.1* (Puebla-Morelos), we eventually confirmed the NE dipping plane as the preferred one, while for *eq3_m6.1* and *eq4_m7.2* we proposed new solutions.

Possible interactions among all the sources were also investigated to find possible causative relationships, through the Coulomb Failure Function analysis (Harris, 1998). However, the stress increase between source combinations does not exceed a few kPa, suggesting the absence of interactions among the sources; this is primarily due to the distances, as already suggested by Chen et al. (2018), about a possible interaction between the M 8.2 Tehuantepec and the M 7.1 Puebla Morelos events. Only the fault responsible for *eq3_m6.1*, the Ixtepec earthquake, experienced a significant increase of 0.1 MPa that, associated with the temporal proximity (14 days) might suggest a causal connection with *eq1_m8.2* (Fig. 4b).
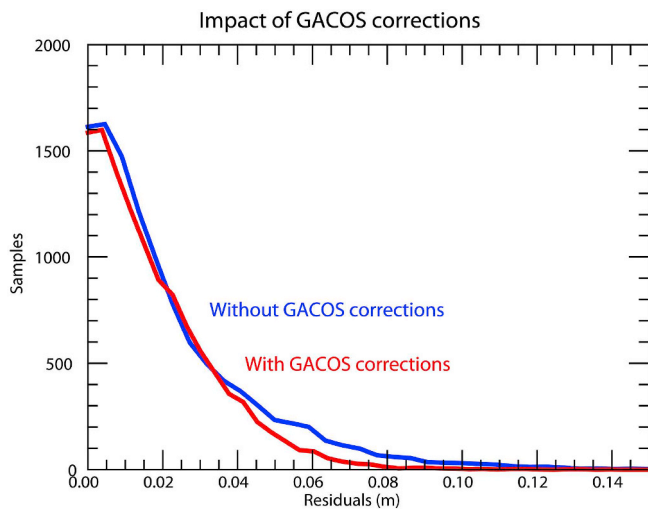
Fig. 6. Comparison between the residual distributions with and without GACOS corrections, for the M 8.2 event.
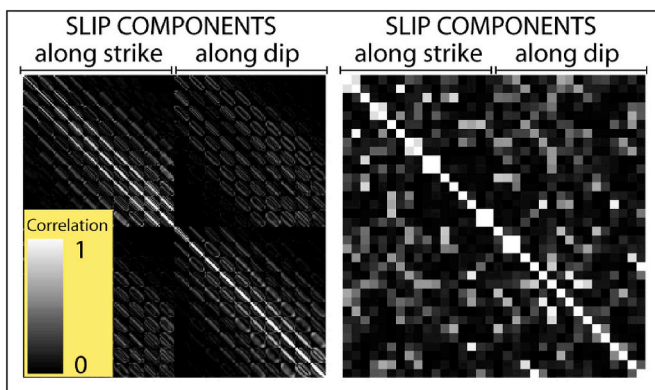

Fig. 7. Comparison between the equally-sized (left) and full-resolution (right) correlations for *eq4_m7.2*, after conducting the linear inversion with variable rake.

6. Conclusions

With the analysis of the four moderate-to-great earthquakes occurred in Mexico between 2017 and 2018 we provided new fault models with unpublished geodetic data and new insights into the analytical source modeling. We investigated the differences between a standard outcome based on the fault subdivision with equally sized patches and that from a full-resolution approach. For the greater events, we extended this algorithm to include the variable rake case.

We show that, although both approaches are equivalent in terms of data fit, the full-resolution algorithm is able to get the same fit with a considerably lower number of parameters, characterized by dimensions which are fully constrained by the observed data. However, the advantages are not merely related to the reduced number of parameters handled in the inversion: the full-resolution algorithm provides a more realistic view of the source responsible for the earthquake, avoiding slip distributions with patterns only driven by *a priori* regularization constraints, and it increases the reliability of the modeled parameters, minimizing the off-diagonal values of the variance-covariance matrix and slip patterns that are only mathematical artifacts.

We also suggest adopting the *norm. spread*(**R**), the normalized Dirichlet Spread Function, as indicator of the resolution obtained with a given fault subdivision; compared to the more diffused checkerboard test, *norm. spread*(**R**) is easy to obtain after any inversion and it quantitatively expresses the quality of the subdivision in terms of resolution.

Appendix A. Supplementary data

Supplementary data to this article can be found online at https://doi.org/10.1016/j.rse.2019.111461.

References

Adriano, B., Fujii, Y., Koshimura, S., Mas, E., Ruiz-Angulo, A., Estrada, M., 2018. Tsunami source inversion using tide gauge and DART tsunami waveforms of the 2017 Mw8.2 Mexico earthquake. Pure Appl. Geophys. 175, 35–48. https://doi.org/10.1007/s00024-017-1760-2.
Atzori, S., Antonioli, A., 2011. Optimal fault resolution in geodetic inversion of coseismic data. Geophys. J. Int. 185, 529–538. https://doi.org/10.1111/j.1365-246X.2011.04955.x.
Biggs, J., Bergman, E., Emmerson, B., Funning, G.J., Jackson, J., Parsons, B., Wright, T.J., 2006. Fault identification for buried strike-slip earthquakes using InSAR: the 1994 and 2004 Al Hoceima, Morocco earthquakes. Geophys. J. Int. 166, 1347–1362. https://doi.org/10.1111/j.1365-246X.2006.03071.x.
Casu, F., Elefante, S., Imperatore, P., Zinno, I., Manunta, M., De Luca, C., Lanari, R., 2014. SBAS-DInSAR Parallel processing for deformation time-series computation. IEEE J. Sel. Top. Appl. Earth Obs. Remote Sens. 7, 3285–3296. https://doi.org/10.1109/JSTARS.2014.2322671.
Cheloni, D., D'Agostino, N., D'Anastasio, E., Avallone, A., Mantenuto, S., Giuliani, R., Mattone, M., Calcaterra, S., Gambino, P., Dominici, D., Radicioni, F., Fastellini, G., 2010. Coseismic and initial post-seismic slip of the 2009 M w 6.3 L'Aquila earthquake, Italy, from GPS measurements. Geophys. J. Int. 181 (3), 1539–1546. https://doi.org/10.1111/j.1365-246X.2010.04584.x.
Chen, K., Feng, W., Liu, Z., Tony Song, Y., 2018. 2017 Mw 8.1 Tehuantepec earthquake: deep slip and rupture directivity enhance ground shaking but weaken the tsunami. Seismol. Res. Lett. 89, 1314–1322. https://doi.org/10.1785/0220170277.
Costantini, M., 1998. A novel phase unwrapping method based on network programming. IEEE Trans. Geosci. Remote Sens. 36, 813–821. https://doi.org/10.1109/36.673674.
Costantini, M., Rosen, P.A., 1999. A generalized phase unwrapping approach for sparse data. IEEE, pp. 267–269. https://doi.org/10.1109/IGARSS.1999.773467.
Custódio, S., Page, M.T., Archuleta, R.J., 2009. Constraining earthquake source inversions with GPS data: 2. A two-step approach to combine seismic and geodetic data sets. J. Geophys. Res. Solid Earth 114. https://doi.org/10.1029/2008JB005746.
De Zan, F., Monti Guarnieri, A., 2006. TOPSAR: Terrain observation by progressive Scans. IEEE Trans. Geosci. Remote Sens. 44, 2352–2360. https://doi.org/10.1109/TGRS.2006.873853.
Dziewonski, A.M., Chou, T.-A., Woodhouse, J.H., 1981. Determination of earthquake source parameters from waveform data for studies of global and regional seismicity. J. Geophys. Res. Solid Earth 86, 2825–2852. https://doi.org/10.1029/JB086iB04p02825.

Ekström, G., Nettles, M., Dziewoński, A.M., 2012. The global CMT project 2004–2010: centroid-moment tensors for 13,017 earthquakes. Phys. Earth Planet. Inter. 200– 201, 1–9. https://doi.org/10.1016/j.pepi.2012.04.002.

Ferrari, L., Orozco-Esquivel, T., Manea, V., Manea, M., 2012. The dynamic history of the Trans-Mexican Volcanic Belt and the Mexico subduction zone. Tectonophysics 522–523, 122–149. https://doi.org/10.1016/j.tecto.2011.09.018.

Fialko, Y., Sandwell, D., Simons, M., Rosen, P., 2005. Three-dimensional deformation caused by the Bam, Iran, earthquake and the origin of shallow slip deficit. Nature 435, 295–299. https://doi.org/10.1038/nature03425.

Funning, G.J., Parsons, B., Wright, T.J., Jackson, J.A., Fielding, E.J., 2005. Surface displacements and source parameters of the 2003 Bam (Iran) earthquake from Envisat advanced synthetic aperture radar imagery. J. Geophys. Res. Solid Earth 110. https://doi.org/10.1029/2004JB003338.

Goldstein, R.M., Werner, C.L., 1998. Radar interferogram filtering for geophysical applications. Geophys. Res. Lett. 25, 4035–4038. https://doi.org/10.1029/1998GL900033.

Gusman, A.R., Mulia, I.E., Satake, K., 2018. Optimum sea surface displacement and fault slip distribution of the 2017 Tehuantepec earthquake (M w 8.2) in Mexico estimated from tsunami waveforms. Geophys. Res. Lett. 45, 646–653. https://doi.org/10.1002/2017GL076070.

Harris, R.A., 1998. Introduction to special section: stress triggers, stress shadows, and implications for seismic hazard. J. Geophys. Res. Solid Earth 103, 24347–24358. https://doi.org/10.1029/98jb01576.

Hayes, G.P., Wald, D.J., Johnson, R.L., 2012. Slab1.0: a three-dimensional model of global subduction zone geometries. J. Geophys. Res. Solid Earth 117https://doi.org/10.1029/2011JB008524. n/a-n/a.

Heidarzadeh, M., Ishibe, T., Harada, T., 2018. Constraining the source of the Mw 8.1 Chiapas, Mexico earthquake of 8 september 2017 using teleseismic and tsunami observations. Pure Appl. Geophys. 175, 1925–1938. https://doi.org/10.1007/s00024-018-1837-6.

Hjörleifsdóttir, V., Singh, S.K., Husker, A., 2016. Differences in epicentral location of Mexican earthquakes between local and global catalogs: an update. Geofísisica Internacional 55, 79–93.

Jarvis, A., Reuter, H.I., Nelson, A., Guevara, E., 2008. In: Hole-filled SRTM for the Globe Version 4, Available from the CGIAR-CSI SRTM 90m Database, . http://srtm.csi.cgiar.org/srtmdata/.

Marquardt, D.W., 1963. An algorithm for least-squares estimation of nonlinear parameters. J. Soc. Ind. Appl. Math. 11, 431–441. https://doi.org/10.1137/0111030.

Massonnet, D., Feigl, K.L., 1998. Radar interferometry and its application to changes in the Earth's surface. Rev. Geophys. 36, 441–500. https://doi.org/10.1029/97RG03139.

Melgar, D., Ruiz-Angulo, A., Garcia, E.S., Manea, M., Manea, V.C., Xu, X., Ramirez-Herrera, M.T., Zavala-Hidalgo, J., Geng, J., Corona, N., Pérez-Campos, X., Cabral-Cano, E., Ramirez-Guzmán, L., 2018a. Deep embrittlement and complete rupture of the lithosphere during the Mw 8.2 Tehuantepec earthquake. Nat. Geosci. 11, 955–960. https://doi.org/10.1038/s41561-018-0229-y.

Melgar, D., Pérez-Campos, X., Ramirez-Guzman, L., Spica, Z., Espíndola, V.H., Hammond, W.C., Cabral-Cano, E., 2018b. Bend faulting at the edge of a flat slab: the 2017 M w 7.1 puebla-morelos, Mexico earthquake. Geophys. Res. Lett. 45, 2633–2641. https://doi.org/10.1002/2017GL076895.

Menke, W., 1989. Geophysical Data Analysis Discrete Inverse Theory. Academic Press, San Diego.

Nevada Geodetic Laboratory, 2019. URL. http://geodesy.unr.edu/index.php accessed 4.22.19.

Page, M.T., Custódio, S., Archuleta, R.J., Carlson, J.M., 2009. Constraining earthquake source inversions with GPS data: 1. Resolution-based removal of artifacts. J. Geophys. Res. Solid Earth 114. https://doi.org/10.1029/2007JB005449.

Pritchard, M.E., Simons, M., Rosen, P.A., Hensley, S., Webb, F.H., 2002. Co-seismic slip from the 1995 July 30 M w = 8.1 Antofagasta, Chile, earthquake as constrained by InSAR and GPS observations. Geophys. J. Int. 150, 362–376. https://doi.org/10.1046/j.1365-246X.2002.01661.x.

Ramírez-Herrera, M.T., Corona, N., Ruiz-Angulo, A., Melgar, D., Zavala-Hidalgo, J., 2018. The 8 september 2017 tsunami triggered by the Mw 8.2 intraplate earthquake, Chiapas, Mexico. Pure Appl. Geophys. 175, 25–34. https://doi.org/10.1007/s00024-017-1765-x.

Reilinger, R.E., Ergintav, S., Burgmann, R., McClusky, S., Lenk, O., Barka, A., Gurkan, O., Hearn, L., Feigl, K.L., Cakmak, R., Aktug, B., Ozener, H., Toksoz, M.N., 2000. Coseismic and postseismic fault slip for the 17 august 1999, M = 7.5, Izmit, Turkey earthquake. Science 289, 1519–1524. https://doi.org/10.1126/science.289.5484.1519.

Sagiya, T., Thatcher, W., 1999. Coseismic slip resolution along a plate boundary megathrust: the Nankai Trough, southwest Japan. J. Geophys. Res. Solid Earth 104, 1111–1129. https://doi.org/10.1029/98JB02644.

Singh, S.K., Ordaz, M., Pacheco, J.F., Quaas, R., Alcantara, L., Alcocer, S., Gutierrez, C., Meli, R., Ovando, E., 1999. A preliminary report on the tehuacan, Mexico earthquake of june 15, 1999 (Mw = 7.0). Seismol. Res. Lett. 70, 489–504. https://doi.org/10.1785/gssrl.70.5.489.

SSN, 2018. Servicio Sismológico nacional, instituto de Geofísica. Universidad Nacional Autónoma de México [WWW Document]. URL. http://www.ssn.unam.mx/doi/networks/mx/ accessed 4.22.19.

USGS, 2017. In: M 8.2 - 101km SSW of Tres Picos, Mexico [WWW Document]. URL. https://earthquake.usgs.gov/earthquakes/eventpage/us2000ahv0#waveform accessed 4.22.19.

USGS, 2018. In: M 7.1 - 1km E of Ayutla, Mexico [WWW Document]. URL. https://earthquake.usgs.gov/earthquakes/eventpage/us2000ar20/finite-fault accessed 4.22.19.

Weston, J., Ferreira, A.M.G., Funning, G.J., 2011. Global compilation of interferometric synthetic aperture radar earthquake source models: 1. Comparisons with seismic catalogs. J. Geophys. Res. 116, B08408. https://doi.org/10.1029/2010JB008131.

Weston, J., Ferreira, A.M.G., Funning, G.J., 2012. Systematic comparisons of earthquake source models determined using InSAR and seismic data. Tectonophysics 532 (535), 61–81. https://doi.org/10.1016/j.tecto.2012.02.001.

Wright, T.J., Lu, Z., Wicks, C., 2003. Source model for the M w 6.7, 23 october 2002, nenana mountain earthquake (Alaska) from InSAR. Geophys. Res. Lett. 30. https://doi.org/10.1029/2003GL018014.

Yu, C., Penna, N.T., Li, Z., 2017. Generation of real-time mode high-resolution water vapor fields from GPS observations. J. Geophys. Res. Atmos. 122, 2008–2025. https://doi.org/10.1002/2016JD025753.

Yu, C., Li, Z., Penna, N.T., 2018. Interferometric synthetic aperture radar atmospheric correction using a GPS-based iterative tropospheric decomposition model. Remote Sens. Environ. 204, 109–121. https://doi.org/10.1016/j.rse.2017.10.038.